INTERNATIONAL JOURNAL OF HYDROGEN ENERGY 50 (2024) 291–304

Available online at www.sciencedirect.com

ScienceDirect

journal homepage: www.elsevier.com/locate/he

Maximum column height and optimum storage depth for geological storage of hydrogen

Mojtaba Ghaedi[*], *Pål Østebø Andersen*, *Raoof Gholami*

Department of Energy Resources, University of Stavanger, Norway

HIGHLIGHTS

- Maximum H_2 column height which avoids capillary breakthrough was formulated.
- Optimum storage depth of hydrogen is approximately 1600 m.
- P10, P50, and P90 for optimum storage depths are 1760, 1565, and 1370 m, respectively.
- A formation with a higher dip angle can offer lower storage capacity for H_2 mass.
- Mixing of gases may lead to lower maximum hydrogen height column.

ARTICLE INFO

Article history:
Received 23 March 2023
Received in revised form
19 June 2023
Accepted 8 July 2023
Available online 22 July 2023

Keywords:
Underground hydrogen storage
Optimum depth
Column height
Structural trapping
Monte-carlo simulation

ABSTRACT

We formulated the maximum hydrogen column height that avoids capillary breakthrough into the caprock above saline aquifers and depleted gas reservoirs. The effects of potential cushion gases such as methane, carbon dioxide, and nitrogen were considered. Using representative rock and fluid properties, the results suggested an optimal depth of approximately 1600 m for hydrogen storage. The use of a cushion gas with a higher density can increase the maximum hydrogen column height and the mass of storable hydrogen. The sensitivity analysis showed that the contact angle and caprock pore radius have the greatest influence on the maximum column height. Uncertainty quantification using Monte-Carlo simulation presented that P10, P50, and P90 for the optimum storage depths are 1760, 1565, and 1370 m, respectively. The mixing of gases resulted in a lower maximum hydrogen height. Moreover, the results indicated a higher dip angle of the formation can decrease the storable hydrogen mass.

Introduction

The hydrogen (H_2) economy as a low-carbon solution will be critical to decarbonizing heavy industry and transitioning to net-zero emissions by 2050 [1–3]. Given the intermittency of renewable resources used to produce green H_2, cost-effective storage options are needed to maintain smart grid stability and balance fluctuations in energy demand [4–7]. H_2 has a very low volume density and as such its storage in salt caverns, saline aquifers, and depleted gas reservoirs has been proposed [8–13]. Salt caverns are perhaps the best option for subsurface H_2 storage, but their main limitations are occurrence of rock salt deposits with suitable depth and thickness [14]. Thus, H_2 storage in porous formations (depleted gas reservoirs and aquifers) has been considered as an alternative to enable large-scale underground H_2 storage.

* *Corresponding author.*
E-mail address: mojtaba.ghaedi@uis.no (M. Ghaedi).

https://doi.org/10.1016/j.ijhydene.2023.07.071

However, special attention should be paid to the sealing capacity of caprock for H_2 storage in porous formations [15–17]. Volume flow (also known as slow Darcy flow) and molecular diffusion are the main reasons behind the gas leakage through the caprock into the adjacent formations under these circumstances [18]. Volume flow is expected to occur when the pressure difference across the caprock becomes greater than the breakthrough (capillary) pressure of the caprock. The diffusion, on the other hand, occurs due to net movement of molecules. Of these two, the volume flow would result in a much larger gas leakage than the molecular diffusion mechanism [19]. In fact, during underground hydrogen storage in porous formations, there is a maximum height of stored hydrogen beneath the caprock that influences structural trapping. Beyond this height, hydrogen can enter the caprock by overcoming the caprock capillary pressure [20].

Few studies have addressed the maximum hydrogen column height (MHCH) and, in turn, evaluated the suitable storage depth for underground hydrogen storage in porous media. Iglauer [20] used a range of rock and fluid properties and calculated the MHCH to prevent capillary breakthrough into the caprock. He reported 1100 m as the depth at which the maximum possible H_2 mass can be stored (also known as the optimum H_2 storage depth (OHSD)). Alessa et al. [21] studied the maximum pressure for H_2 storage in gas reservoirs at which capillary breakthrough of the caprock is avoided. They indicated that safe storage of H_2 in a structural trap is possible at least at a pressure equal to the original methane pressure. Luboń & Tarkowski [22] simulated H_2 injection into the deep Suliszewo aquifer structure in northwestern Poland. They considered the effects of capillary and fracturing pressure and determined a depth of 1200–1400 m as the OHSD based on the maximum working gas capacity. They concluded that the shift of the OHSD from 1100 m previously calculated by Iglauer [20], was due to the geological characteristics of the Suliszewo structure.

In this paper, we evaluate the MHCH in geological porous formations (aquifers and gas reservoirs). In particular, the impacts of other base gases such as remaining hydrocarbon gas, nitrogen (N_2) and carbon dioxide (CO_2) are considered. In addition, OHSDs are calculated based on the maximum mass of H_2 that can be stored. A Monte Carlo simulation is also performed to qualify the uncertainties and a sensitivity analysis is conducted on the effective parameters. Moreover, the side effects of gas mixing and formation dip angle on the MHCH are investigated. The rest of the paper is structured as follows: the formulation of MHCH in porous formations is presented, followed by the rock and fluid properties. The results of H_2 storage in aquifers and depleted gas reservoirs are presented, followed by Monte Carlo simulation and sensitivity analysis. Finally, the effect of the formation dip angle is investigated.

Formulation

Fig. 1a shows a general case for underground H_2 storage in a subsurface porous medium, where, in addition to water and injected H_2, other gases such as N_2 and CO_2 may be injected as base gases. Additionally, in depleted gas reservoirs, remaining hydrocarbon gas also exists. Depending on the volume and density, each of the injected or existing gases occupies a certain height in the subsurface formation in order from low density at the top to high density at the bottom (Fig. 1b).

A force balance can then be established over the entire gas column between buoyancy, gravity, and capillary forces in the formation during underground H_2 storage:

$$\text{Buoyancy force} - \text{Gravity force} = \text{Capillary force} \tag{1}$$

The buoyancy force acts upwards and corresponds to the weight of the displaced water. As long as the net difference between the buoyancy force and gravity is less than the capillary threshold force of the caprock, a volume flow is not expected. The magnitude of the buoyancy force can be quantified using Eq. (2):

$$\begin{aligned}\text{Buoyancy force} &= \rho_W\left(V_{H_2} + V_{N_2/CO_2} + V_G\right)g \\ &= \rho_W A\phi(1 - S_w)\left(h_{H_2} + h_{N_2/CO2} + h_G\right)g\end{aligned} \tag{2}$$

where, ρ_W is the water density, V_{H_2} is the volume of injected H_2, V_{N_2/CO_2} represents the volume of injected N_2 or CO_2, V_G denotes the volume of hydrocarbon gas, g is the gravitational constant, ϕ is porosity, A is the cross sectional area, h_{H_2} is the H_2 height, h_{N_2/CO_2} is the N_2 or CO_2 height, h_G is the hydrocarbon gas height, and S_w is the water saturation in the H_2 plume. The

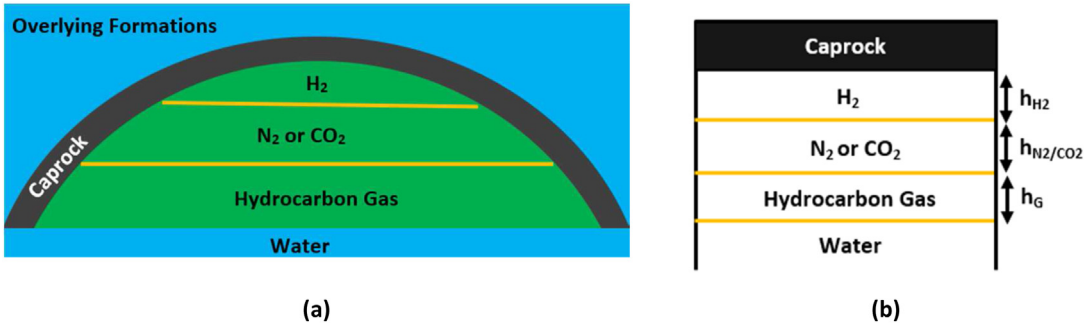

Fig. 1 – (a) A Schematic view of underground H_2 storage in presence of different fluids and (b) the simplified representation of column height in the storage site.

downward gravitational force, on the other hand, can be addressed as:

$$\text{Gravity force} = \left(\rho_{H_2} V_{H_2} + \rho_{N_2/CO_2} V_{N_2/CO_2} + \rho_G V_G\right) g = A\phi(1 - S_w)\left(\rho_{H_2} h_{H_2} + \rho_{N_2/CO_2} h_{N_2/CO_2} + \rho_G h_G\right) g \quad (3)$$

where, ρ_{H_2} is the H_2 density, ρ_{N_2/CO_2} is the N_2 or CO_2 density, and ρ_G is the hydrocarbon gas density. The Laplace equation can then be used to formulate the capillary force between the H_2 plume and the water in the caprock, which is written as [23]:

$$\text{Capillary force} = \frac{2\gamma_{H_2,W}\cos(\theta_{H_2,W})}{r} A\phi(1 - S_w) \quad (4)$$

where, $\gamma_{H_2,W}$ is the interfacial tension between H_2 and water, $\theta_{H_2,W}$ is the H_2-water contact angle, and r is the pore size radius.

Substituting Eqs. (2)–(4), into Eq. (1) and rearranging it based on h_{H_2} gives:

$$h_{H_2} = \frac{2\gamma_{H_2,W}\cos(\theta_{H_2,W})}{gr(\rho_W - \rho_{H_2})} - h_{N_2/CO_2}\frac{\rho_W - \rho_{N_2/CO_2}}{\rho_W - \rho_{H_2}} - h_G\frac{\rho_W - \rho_G}{\rho_W - \rho_{H_2}} \quad (5)$$

Some of the injected H_2 may act as base/cushion gas. Thus, one can further split h_{H_2} into height of working H_2 ($h_{working,H_2}$) and base (h_{base,H_2}) gas:

$$h_{H_2} = h_{working,H_2} + h_{base,H_2} \quad (6)$$

Therefore, Eq. (6) can be reformulated as:

$$h_{working,H_2} = \frac{2\gamma_{H_2,W}\cos(\theta_{H_2,W})}{gr(\rho_W - \rho_{H_2})} - h_{N_2/CO_2}\frac{\rho_W - \rho_{N_2/CO_2}}{\rho_W - \rho_{H_2}} - h_G\frac{\rho_W - \rho_G}{\rho_W - \rho_{H_2}} - h_{base,H_2} \quad (7)$$

Eq. (7) can be used to estimate the MHCH below the caprock. In this work, this equation is used to obtain $h_{working,H_2}$ under different conditions during underground H_2 storage in aquifers or depleted gas reservoirs. To calculate MHCH, rock and fluid properties are evaluated at the targeted depth of the reservoir top and the fluid densities are assumed to be constant within the column height.

Based on Eq. (7), depending on rock and fluid properties, $h_{working,H_2}$ can vary at different formation top depths. The mass of storable working H_2 (m) could also be different at various formation top depths. Thus, assuming a constant A and a constant ϕ as a function of depth, the storable mass of working H_2 per unit of effective pore area (m^*) can be formulated as:

$$m^* = \frac{m}{A\phi(1 - S_w)} = \rho_{H_2} h_{working,H_2} \quad (8)$$

As stated before, the depth at which a maximum m^* can be stored is defined as the OHSD [20,24].

The base gas for underground H_2 storage in saline aquifers can be H_2 itself, N_2 or CO_2. If the base gas is neither N_2 nor CO_2 ($h_{N_2/CO_2} = 0$ and $h_G = 0$), H_2 itself can serve as the base gas and Eq. (7) is simplified to:

$$h_{working,H_2} = \frac{2\gamma_{H_2,W}\cos(\theta_{H_2,W})}{gr(\rho_W - \rho_{H_2})} - h_{base,H_2} \quad (9)$$

On the other hand, in aquifers if the choice of the base gas is either N_2 or CO_2, H_2 acts as the working gas ($h_G = 0$ and $h_{base,H_2} = 0$) and Eq. (7) can be expressed as:

$$h_{working,H_2} = \frac{2\gamma_{H_2,W}\cos(\theta_{H_2,W})}{gr(\rho_W - \rho_{H_2})} - h_{N_2/CO_2}\frac{\rho_W - \rho_{N_2/CO_2}}{\rho_W - \rho_{H_2}} \quad (10)$$

It should be kept in mind that in gas storage operations, about 40–70% of the gas can serve as base gas [25]. In this study, a 50% ratio was used and as such the volume of working and base gas was considered the same in different analysis.

For H_2 storage in gas reservoirs, the remaining hydrocarbon gas in the reservoir at the beginning of the storage operation can play a role as part of the required base gas. Here, we considered different conditions where the remaining hydrocarbon gas serve as a base gas either with H_2, N_2 or CO_2. If CH_4 is considered as a representative gas for the remaining hydrocarbon gas in the reservoir and only H_2 is assumed as another part of the base gas ($h_{N_2/CO_2} = 0$), Eq. (7) can be shortened as follows:

$$h_{working,H_2} = \frac{2\gamma_{H_2,W}\cos(\theta_{H_2,W})}{gr(\rho_W - \rho_{H_2})} - h_{CH_4}\frac{\rho_W - \rho_{CH_4}}{\rho_W - \rho_{H_2}} - h_{base,H_2} \quad (11)$$

However, If N_2 or CO_2 is assumed to be the base gas together with CH_4 (i.e., $h_{base,H_2} = 0$), Eq. (7) can be expressed as:

$$h_{working,H_2} = \frac{2\gamma_{H_2,W}\cos(\theta_{H_2,W})}{gr(\rho_W - \rho_{H_2})} - h_{N_2/CO_2}\frac{\rho_W - \rho_{N_2/CO_2}}{\rho_W - \rho_{H_2}} - h_{CH_4}\frac{\rho_W - \rho_{CH_4}}{\rho_W - \rho_{H_2}} \quad (12)$$

To predict $h_{working,H_2}$ and m^* under different circumstances, the rock and fluid properties (threshold radius, fluid densities, contact angle and interfacial tension) should be known. The next section discusses the procedure and relationships that can be used to calculate these properties.

Rock and fluid properties

As mentioned earlier, $h_{working,H_2}$ and consequently m^* depend on the rock and fluid properties. With the exception of r, the other properties required to calculate $h_{working,H_2}$ and m^* must be evaluated as functions of depth since they depend on pressure and temperature. Thus, a tabulated dataset was created for each property at different pressures and temperatures. Assuming normal pressure and temperature gradients (P_G and T_G), the values of the properties were determined as a function of depth. In this work, we assumed 0.01 MPa/m and 0.03 °C/m for P_G and T_G, respectively and used MATLAB [26] software for two-dimensional interpolation of the properties as functions of temperature and pressure.

The magnitude of the capillary force is inversely proportional to the pore radius (r) of caprock. Therefore, a very tight caprock offers a stronger capillary force against the buoyancy force exerted by the hydrogen column in a storage site. Shale is a common seal in different geological structures with an

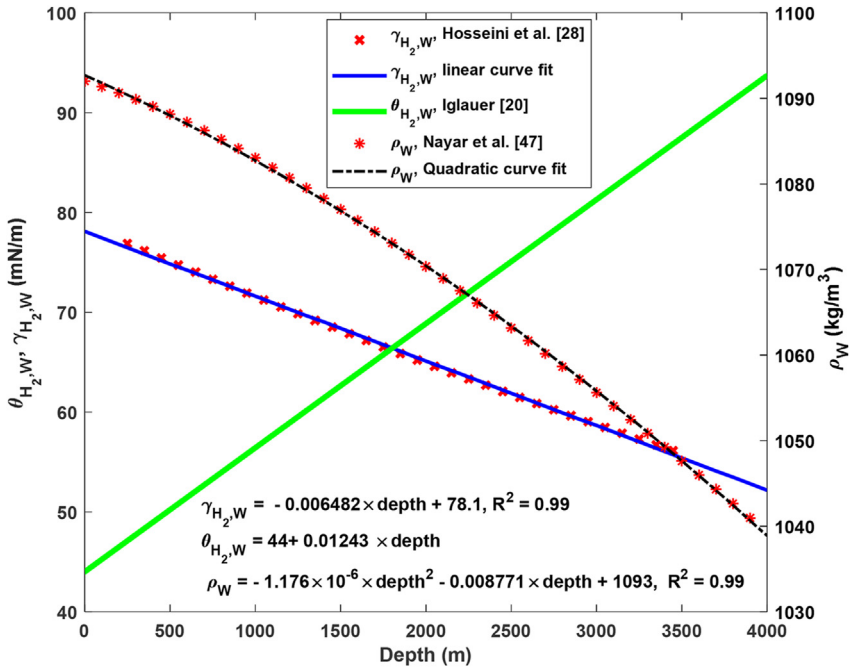

Fig. 2 – γ_{H_2-W} together with linear curve fit, $\theta_{H_2,W}$, and ρ_W vs. depth.

average pore size of 5 nm–100 nm [23]. Thus, a pore radius of 50 nm was assumed as a representative base value for the caprock which has also been suggested by other studies [20,24].

The interfacial tension between hydrogen and water ($\gamma_{H_2,W}$) is a function of temperature, pressure, and salinity [27,28]. It has been reported that $\gamma_{H_2,W}$ decreases linearly with increasing temperature or pressure and increases linearly with increasing salinity [28]. Several studies have experimentally investigated the variation of $\gamma_{H_2,W}$ by temperature, pressure and salinity [15,27–29]. For example, Hosseini et al. [28] recently studied the effects of temperature, pressure, and salinity on the $\gamma_{H_2,W}$ and developed a correlation to calculate $\gamma_{H_2,W}$. In this study, we used their correlation to calculate $\gamma_{H_2,W}$, the details of which are given in Appendix A. Fig. 2 shows the linear decrease of $\gamma_{H_2,W}$ as a function of depth together with the linear curve fit.

The hydrogen-brine contact angle ($\theta_{H_2,W}$) plays an important role in geological storage. In fact, if $\theta_{H_2,W}$ is greater than 90° during the injection or storage, water will be displaced by H_2 and capillary leakage may occur [30]. Experimental studies have been performed to study the impacts of temperature, pressure, rock minerology, salinity, surface roughness and organic acid concentration on $\theta_{H_2,W}$ [31–35]. In particular, for caprock, it has been reported that $\theta_{H_2,W}$ increases with increasing pressure and increasing concentration of organic acid but decreases with increasing temperature [15]. In addition, the optimal conditions with the lower risk of underground H_2 storage in carbonate formations appeared to be low salinity, low pressure, low organic acid concentration, and high temperature [36]. Ali et al. [37] highlighted the important role of organic acid on caprock wettability. They showed that mica substrates tend to become H_2 wet as a result of organic

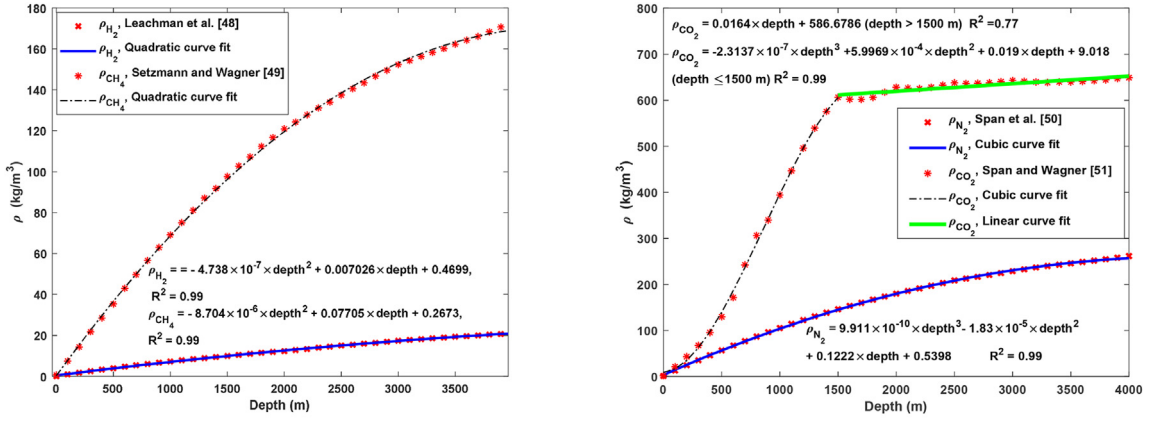

Fig. 3 – Density of gases vs. depth with curve fit lines: (a) ρ_{H_2} and ρ_{CH_4} (b) ρ_{N_2} and ρ_{CO_2}.

Table 1 – Properties of the base case.

Parameter	Value	Unit
P_G	0.01	MPa/m
T_G	0.03	°C/m
r	50	nm
$\gamma_{H_2,W}$	Fig. 2	mN/m
$\theta_{H_2,W}$	Fig. 2	–
ρ_W	Fig. 2	kg/m^3
ρ_{H_2}	Fig. 3a	kg/m^3
ρ_{N_2}	Fig. 3b	kg/m^3
ρ_{CO_2}	Fig. 3b	kg/m^3

acid. Similarly, other studies emphasized that the caprock wettability is a strong function of organic acid content [38–40]. Thus, the capillary sealing capacity of a caprock may be overestimated if the presence of organic acid is ignored. Recently, it has been shown that Alumina nanofluid has a great potential to improve the wettability of organically aged mica samples as a proxy of caprock [39]. Alanazi et al. [40] studied the impacts of gas mixing on the wettability using Jordanian oil shale rocks. They reported higher contact angle for the H_2–CH_4 mixture compared to H_2.

Furthermore, gas-rock interfacial tension is a very important parameter to examine the sealing capacity of a caprock. Lower values for gas-caprock interfacial tension shows a stronger affinity of the gas to the caprock surface and consequently a higher possibility of gas leakage [41]. Efforts have been made to investigate the behavior of the rock-H_2 interfacial tension as a function of temperature, pressure, salinity, total organic carbon, and rock minerology. Esfandyari et al. [42] reported that rock-H_2 interfacial tension is a strong function of rock lithologies such as calcite, dolomite, quartz, shale, anhydrite, gypsum, granite, and basalt. They found that the value of the rock-H_2 interfacial tension decreases with increasing pressure but increases with increasing salinity. They also reported that the impacts of temperature on rock-H_2 interfacial tension are different and depend on the rock minerology. Another study revealed that under similar thermodynamic conditions, the clay-H_2 interfacial tension is larger than that of clay-N_2 and clay-CO_2 and different clay compositions do not have a considerable influence on the clay-H_2 interfacial tension [43]. Additionally, a decrease in the rock-H_2 interfacial tension with increasing total organic carbon was presented for shale, evaporite, and basaltic rocks [44]. It has also been reported that H_2 adsorption decreases strongly with increasing total organic carbon [45].

Iglauer [20] assumed 0.01 mol/lit steric acid concentration and described the increase of $\theta_{H_2,W}$ from 44° at the surface (0 m depth) to 92° at 4000 m depth (specifically 90° at 3700 m depth). He explained that the trend of $\theta_{H_2,W}$ as a function of depth is due to the fact that H_2 density increases with depth, resulting in stronger intermolecular interactions between H_2 and rock. This trend and the relationship between the contact angle and depth are shown in Fig. 2.

Higher value of ρ_w increases the buoyancy force magnitude. It should be noted that ρ_w depends on temperature, pressure, and salinity. Different correlations have been developed to estimate the ρ_w in different temperature, pressure, and salinity ranges [46]. The correlation proposed by Nayar et al. [47] was used in this work to determine ρ_w as a function of depth. They developed their correlation using available experimental data from the literature. This correlation was selected because it is valid for a wider range of temperature (10–120 °C) and salinity (0–120 g/kg). The range of validity of this correlation for pressure is 0–12 MPa, but it should be noted that ρ_w is not much affected by pressure [46]. Thus, this correlation was also used for higher pressure conditions. Appendix A presents the correlation developed by Nayar et al. [47] to calculate ρ_w. In this paper, a salinity of 120 g/kg was assumed as the average salinity of the water to determine ρ_w. Thus, the average salinity of the formation water is consistent with the value used for the caprock. Fig. 2 also shows the interpolated ρ_w versus depth along with the quadratic curve fit line.

In this part, the relationships for ρ_{H_2}, ρ_{CH_4}, ρ_{N_2}, and ρ_{CO_2} (densities of working- and base gases) are presented. CH_4 was selected to represent hydrocarbon gas and therefore ρ_G and h_G are replaced by CH_4 density (ρ_{CH_4}) and CH_4 height (h_{CH_4}), respectively, in the previously mentioned equations (Eqs. (2), (3), (5), and (7)). To calculate gas densities, the previous

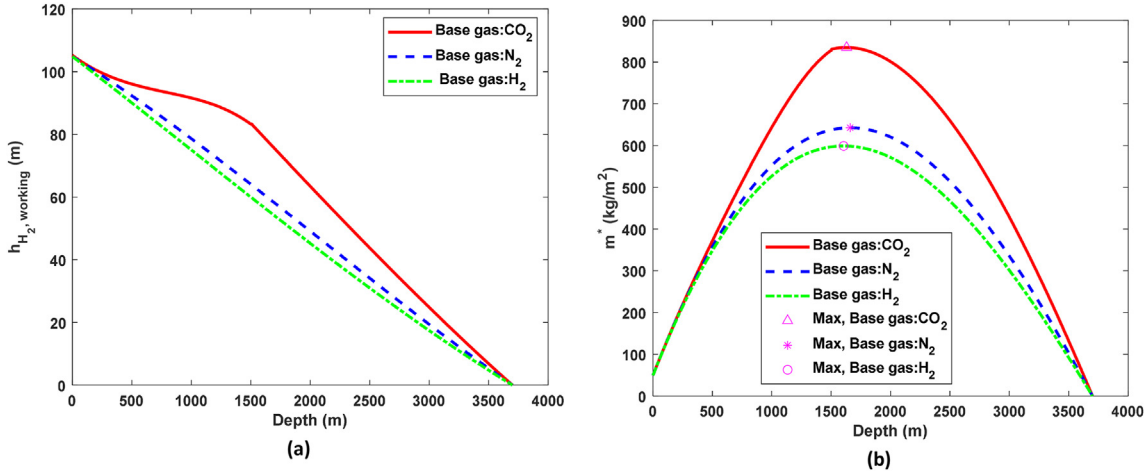

Fig. 4 – H_2 storage in aquifers using different base gases including CO_2, N_2, and H_2 itself: (a) $h_{working,H_2}$ vs. depth (b) and m^* vs. depth.

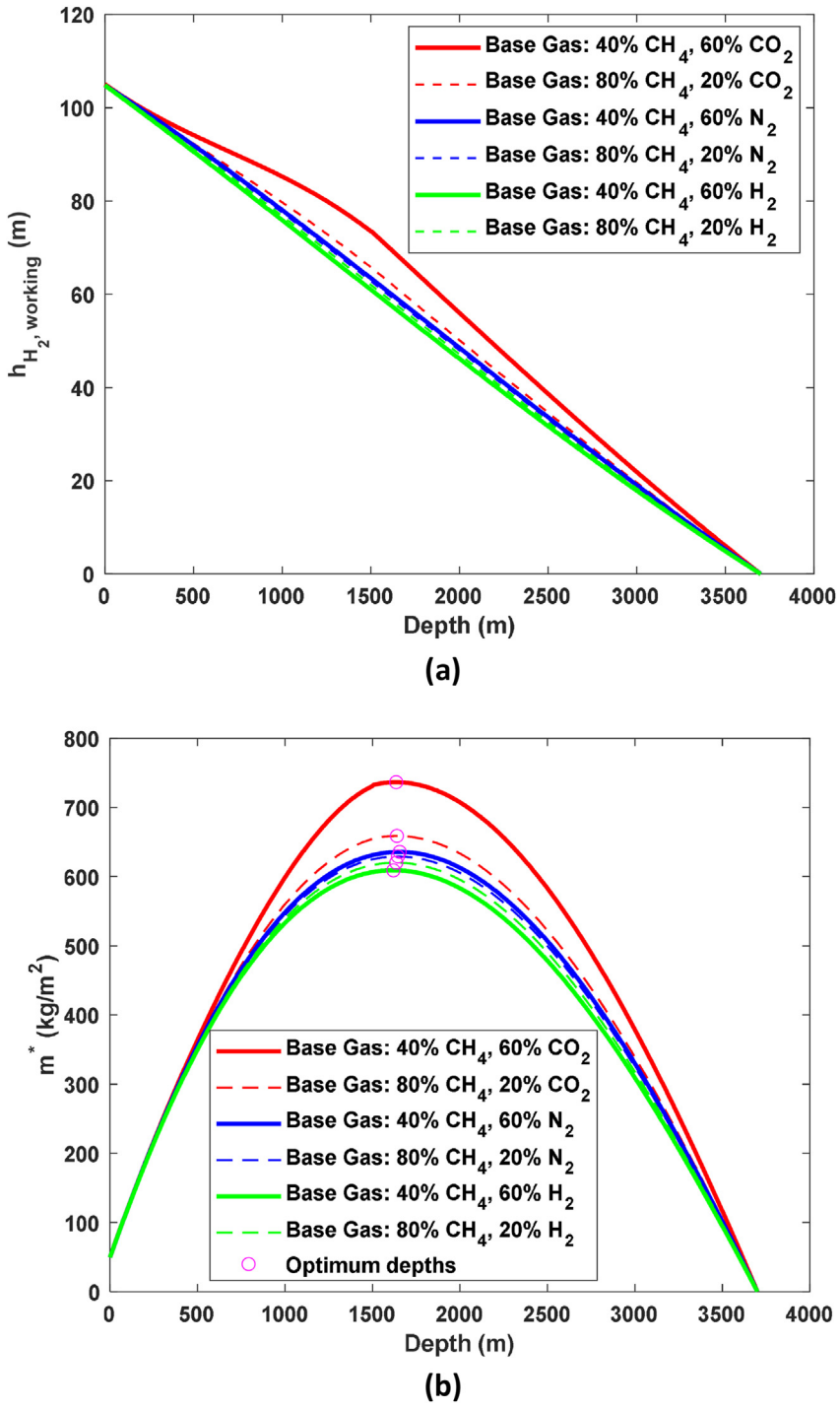

Fig. 5 – H_2 storage in gas reservoirs using different base gases including CO_2, N_2, and H_2 itself: (a) $h_{working.H_2}$ vs. depth (b) m^* vs. depth.

works which provided a desirable gas density in a wide range of temperature and pressure were considered. Fig. 3a shows ρ_{H_2} vs. depth and the quadratic curve fit line. The ρ_{H_2} data at different temperatures and pressures published by Leachman et al. [48] were used to interpolate ρ_{H_2} vs. depth. ρ_{H_2} changes from 0.085 kg/m^3 at the surface to 21 kg/m^3 at 4000 m depth. Similarly, Fig. 3a also shows ρ_{CH_4} as a function of depth, where the data provided by Setzmann and Wagner [49] were used for interpolation.

Fig. 3b shows ρ_{N_2} and ρ_{CO_2} against depth. The Interpolation of ρ_{N_2} was based on data from Span et al. [50] and ρ_{CO_2} was determined using data from Span and Wagner [51]. The value of ρ_{CO_2} increases significantly with depth and shows an almost linear increase with depth after 1500 m, which is consistent with previous work [24]. Considering the critical temperature and pressure of CO_2, 31.1 °C and 7.38 MPa, respectively, CO_2 could be in a supercritical state at certain depths depending on P_G and T_G. In this state, liquid and gaseous phases are

indistinguishable, and CO_2 has a density similar to that of a liquid [52]. Based on Fig. 3, one can conclude that the variation of gas densities with depth will be $\rho_{H_2} < \rho_{CH_4} < \rho_{N_2} < \rho_{CO_2}$.

Looking at Fig. 3, certain discrepancies are observed between the interpolated density points and the curve fitting lines at the surface or at the depth of the reservoir at about 4000 m depth. It should be mentioned that these differences do not have a significant impact on the calculation, as these densities are subtracted from ρ_w in the $h_{working,H_2}$ formula. Moreover, H_2 storage near the surface (due to the unavailability of such geological formations) or very deep in the reservoir (due to wettability and the possibility of capillary leakage) may not be the interest of underground H_2 storage.

Results and discussion

In this section, we examine the MHCH and OHSD in saline aquifers and depleted gas reservoirs. In particular, the presence and absence of N_2 and CO_2 as base gas is evaluated. In addition, uncertainties are quantified by Monte Carlo simulations, sensitivity analyses are performed and the effects of PG and TG as well as the inclination (dip) angle of the formation are analyzed.

H_2 storage in saline aquifers

To evaluate MHCH and OHSD in saline aquifers, a base case was considered. Table 1 gives the parameters of the base case. With the given rocks and fluids properties and Eqs. (8)–(10), the MHCH was calculated as a function of depth. In this work, we have assumed that the formation pressure after the injections (base and working gas) reaches the pressure defined by normal PG at that depth. Fig. 4 shows the $h_{working,H_2}$ and m^* as a function of depth for H_2 storage in aquifers when different base gases such as CO_2, N_2, and H_2 were used. As can be seen in Fig. 4a, $h_{working,H_2}$ decreases from 104 m at the surface to 0 at 3700 m depth, where $\theta_{H_2,W}$ becomes 90°. It should be noted that the height of the base gas at any depth is the same height as $h_{working,H_2}$. From Eq. (7), it can be concluded that using a base gas with a higher density leads to a higher $h_{working,H_2}$ and consequently to a higher m^*. In fact, a higher gas density increases the magnitude of gravity force against the buoyancy force. At shallow depths, all gases have low density compared to ρ_w and at deep depths, $h_{working,H_2}$ approaches 0 due to wettability conditions. Thus, $h_{working,H_2}$ and m^* of CO_2 are larger than those of N_2 and H_2, except at shallow and deep depths. Fig. 4b shows that the OHSD for H_2, N_2, and CO_2 is 1605, 1660, and 1630 m, respectively. Moreover, the optimum m^* of the case with CO_2 as the base gas is 835 kg/m^2, which is 30 and 39% more than the optimum m^* of the cases with N_2 (643 kg/m^2) and H_2 (599 kg/m^2) as the base gas, respectively.

H_2 storage in gas reservoirs

To calculate $h_{working,H_2}$ and m^* as a function of depth in depleted gas reservoirs, the rock and fluid properties presented earlier were used together with Eqs. (8), (11) and (12). Two different conditions were considered where the contributions of CH_4 were 40 and 80% of the total base gas height. While the 40% scenario represents the condition where the gas reservoir is almost depleted to its ultimate recovery factor, the 60% scenario shows the situation where some recoverable hydrocarbon gas may still be present in the reservoir at the beginning of H_2 storage. Fig. 5 shows the variation of $h_{working,H_2}$ and m^* as a function of depth for H_2 storage in a depleted gas reservoir.

As can be seen in Fig. 5, the trends of the various base gases are similar to those observed in the aquifer. It seems that the height of the working gas with CO_2 as the base is generally greater than that of N_2 and that is greater than the height of H_2. A similar comparison can be made for m^*. For the condition with H_2 as the base gas, the case with 80% CH_4 provides slightly higher $h_{working,H_2}$ and m^* compared to the case with 40%. This could be linked to the fact that a denser base gas offers a higher MHCH. The results are different when CO_2 is used with CH_4 as the base gas. CO_2 is denser than CH_4 and the case where the base gas is mainly CO_2 (60% of the height of the base gas is CO_2) gives higher $h_{working,H_2}$ and m^*. Compared to the differences in the densities of CH_4 with H_2 and CO_2, the

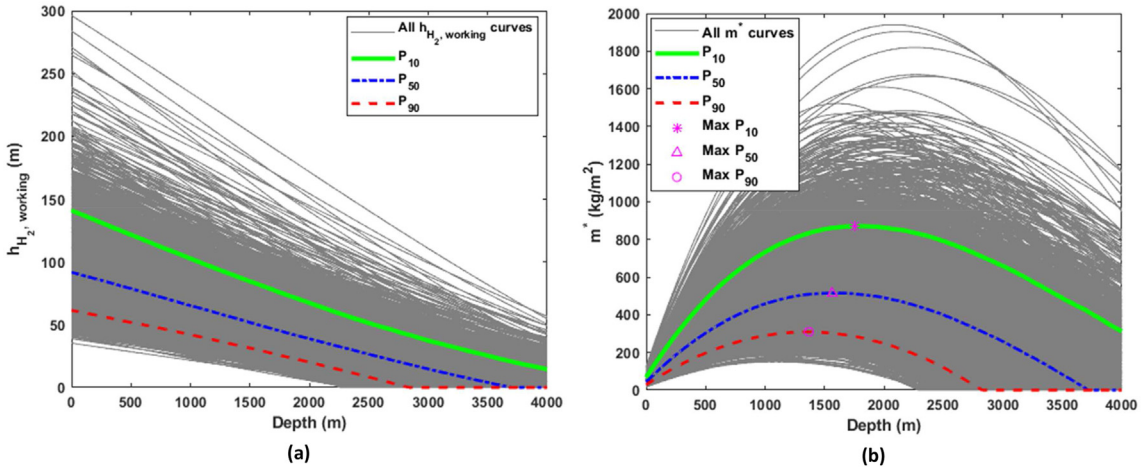

Fig. 6 – Monte Carlo simulation results for all cases together with P10, P50, and P90 curves: (a) $h_{working,H_2}$ vs. depth (b) and m^* vs. depth.

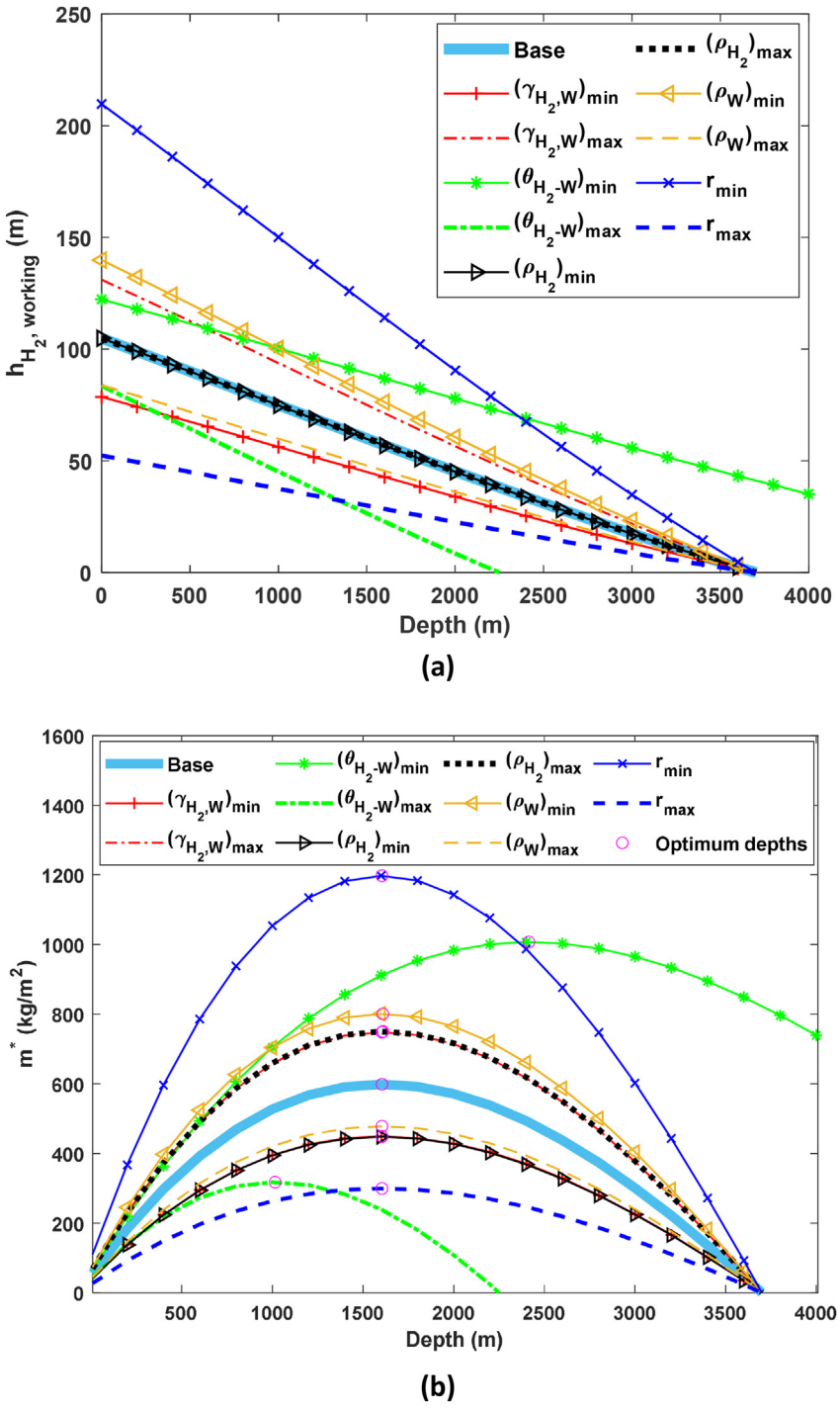

Fig. 7 – Sensitivity analysis of the impacts of parameters r, $\gamma_{H_2,W}$, $\theta_{H_2,W}$, ρ_w and ρ_{H_2} on: (a) $h_{working,H_2}$ vs. depth (b) and m^* vs. depth.

densities of CH_4 and N_2 are not significantly different. Therefore, when N_2 is the base gas, the two cases with 40% and 80% CH_4 give almost similar results. Looking at Fig. 5b, it can be concluded that the OHSDs were not noticeably affected by the contribution of CH_4 in the base gas when compared to those of the aquifers for different base gases.

It should be noted that it is possible for base and working gases to mix in an underground H_2 storage [53]. Appendix B shows the effects of this mixing on $h_{working,H_2}$ and m^*. The results show that mixing between N_2 and CH_4 does not change $h_{working,H_2}$ and m^*, but mixing N_2 with H_2 leads to a slight decrease in the values of $h_{working,H_2}$ and m^*. A stronger decrease of $h_{working,H_2}$ and m^* was observed when CO_2 was mixed with CH_4 and especially with H_2.

Uncertainty quantification and sensitivity analysis

In this section, we provide an uncertainty assessment using Monte Carlo simulation and perform a sensitivity analysis of the effective parameters in a geological storage site. The analysis is performed for the base case (Table 1) where there is no N_2, CO_2, or hydrocarbon gas and H_2 acts as the base gas ($h_{N_2/CO_2} = 0$, $h_G = 0$ and $h_{base,H_2} \neq 0$ (Eq. (9))).

Monte Carlo simulation is widely used in the oil and gas industry to quantify uncertainties associated with the estimation of hydrocarbon in place or production analysis [54–56]. The parameters in Eqs. (8) and (9), i.e., r, $\gamma_{H_2,W}$, $\theta_{H_2,W}$, ρ_w, and ρ_{H_2}, may be uncertain due to different factors such as changes in P_G,T_G, minerology, and salinity. We assumed a triangular distribution for these parameters given the limited number of data samples [57]. Except for the parameter r, the values reported earlier for the different parameters were used as the mode and 25% more and less than the mode were considered for the maximum and minimum in the triangular distributions, respectively. For the parameter r, which was assumed to be constant as a function of depth, a triangular distribution was considered with a mode, maximum, and minimum of 50, 100, and 25 nm, respectively. It should be mentioned that the values of r are prone to higher variations and as such a wider range was considered for this parameter. For each of the other parameters, i.e., $\gamma_{H_2,W}$, $\theta_{H_2,W}$, ρ_w and ρ_{H_2}, which are assumed to be a function of depth, triangular distributions were assumed for multiplying factors with a mode, maximum, and minimum of 1, 1.25, and 0.75, respectively. In each of the Monte Carlo simulation cases, the randomly selected multiplication factor from the corresponding triangular distribution of a parameter is multiplied by that parameter to obtain a new pattern as a function of depth. In the Monte Carlo simulation, 10,000 simulation cases were used to obtain almost stable simulation results. The individual steps of performing the Monte Carlo simulation are described below:

1. For each of the simulation cases:
   a. Select random values for r and multiplying factors from the corresponding distribution functions of the parameters $\gamma_{H_2,W}$, $\theta_{H_2,W}$, ρ_w and ρ_{H_2}.
   b. Determine the new trends for the parameters $\gamma_{H_2,W}$, $\theta_{H_2,W}$, ρ_w and ρ_{H_2} using the randomly selected multiplying factors.
   c. Calculate $h_{working,H_2}$ and m^*.
2. For depths from 0 to 4000 m:
   a. Calculate the cumulative distribution function (CDF) and then the complementary cumulative distribution function (CCDF with CCDF = 1 - CDF) for the results obtained for $h_{working,H_2}$ and m^*. Read the values of P10, P50, and P90 for $h_{working,H_2}$ and m^* from the generated CCDF.

Fig. 6 shows the results of the Monte Carlo simulation for all simulation cases together with P10, P50, and P90 of $h_{working,H_2}$ and m^* as a function of depth. As can be seen in Fig. 6, the OHSDs of P10, P50, and P90 are 1760, 1565, and 1370 m, respectively. This means that in 90% of the simulation cases, the OHSD is greater than 1370 m and only in 10% of the cases, the OHSD is greater than 1760 m. Furthermore, m^* at the OHSDs of P10, P50, and P90 are 872, 515, and 310 kg/m^2, respectively. Thus, in 90% of the simulation cases, m^* is greater than 310 kg/m^2. It is worth noting that the P90 value obtained for the OHSD is consistent with the 1200–1400 m OHSD reported for the Suliszewo deep aquifer [22].

To perform the sensitivity analysis, we modified one parameter at a time between its maximum and minimum. The parameters considered were the same as those used in the Monte Carlo simulation (r, $\gamma_{H_2,W}$, $\theta_{H_2,W}$, ρ_w and ρ_{H_2}). The maximum and minimum values for the different parameters were also the same as the Monte Carlo simulation. Fig. 7 shows the sensitivity analysis of the effects of the parameters including r, $\gamma_{H_2,W}$, $\theta_{H_2,W}$, ρ_w and ρ_{H_2} on $h_{working,H_2}$ and m^*. In particular, Fig. 8 presents the influences of the mentioned parameters on OHSD and m^* at the optimum depth. Comparing the obtained values from the minimum and maximum scenarios with the base case (dashed line), it can be seen that $\theta_{H_2,W}$ is the only parameter that affects the OHSD (Fig. 8a). It should be noted that although the OHSD is not

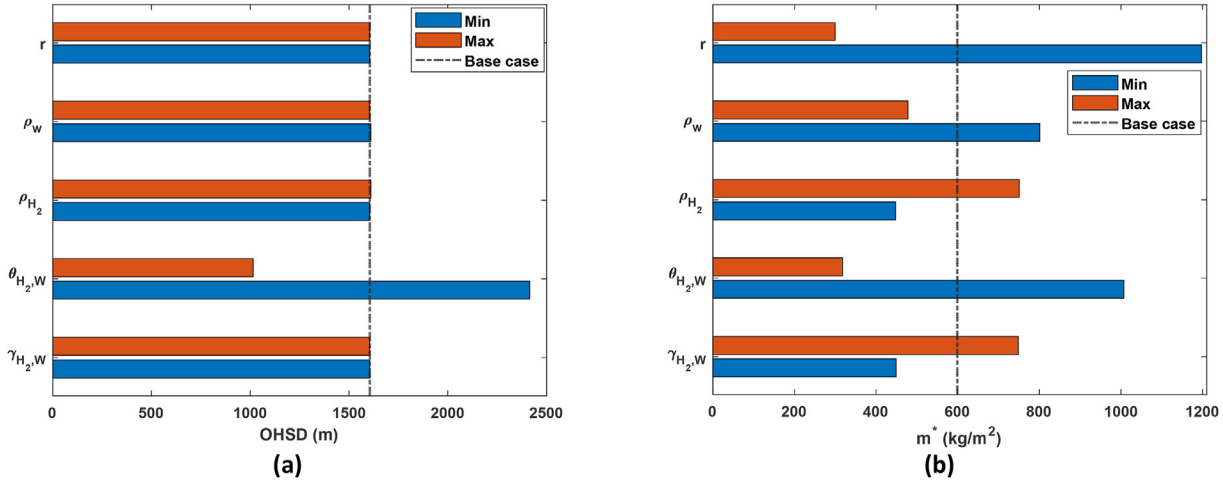

Fig. 8 – The impacts of the uncertain parameters (r, $\gamma_{H_2,W}$, $\theta_{H_2,W}$, ρ_w) and ρ_{H_2} on (a) OHSD and (b) m^*.

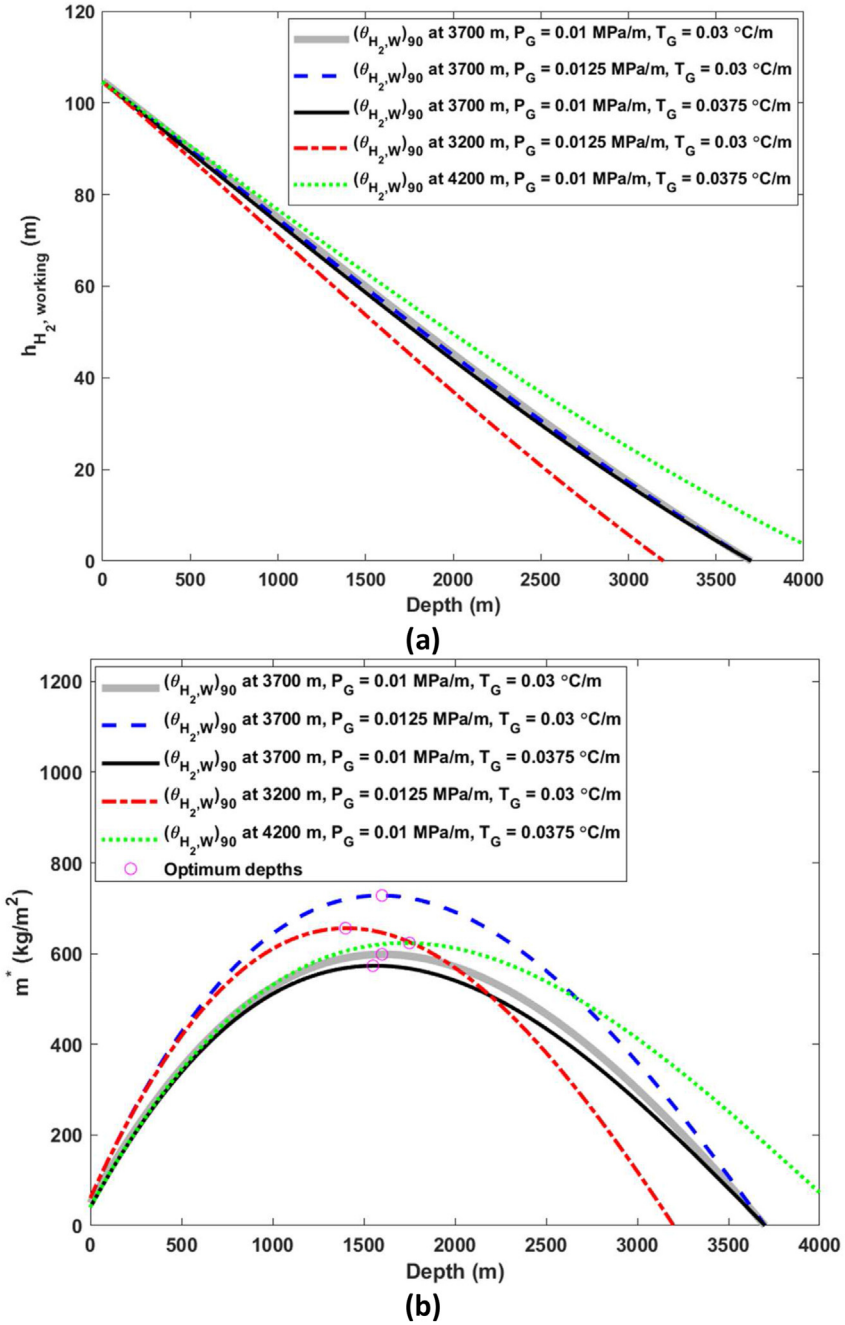

Fig. 9 – The influences of T_G and P_G together with $\theta_{H_2,W}$ profiles on: (a) $h_{working,H_2}$ vs. depth (b) m^* vs. depth.

affected by the change in the other parameters, including r, $\gamma_{H_2,W}$, ρ_w and ρ_{H_2}, the magnitude of m^* is affected by these parameters (Fig. 7b and 8b). It must be emphasized that the magnitude of $h_{working,H_2}$ and hence m^* is a function of $\cos(\theta_{H_2,W})$ and not of $\theta_{H_2,W}$. Thus, a 25% variation of $\theta_{H_2,W}$, affects the values of m^* differently from the other parameters. Furthermore, the considerable impacts of r on $h_{working,H_2}$ and m^* should be noted. As expected, minimum values of r (higher capillary force), ρ_w (lower buoyancy force), and $\theta_{H_2,W}$ (higher capillary force) result in higher values of m^* at the OHSD compared to the base case. On the other hand, maximum values of $\gamma_{H_2,W}$ (higher capillary force) and ρ_{H_2} (higher H_2 mass and gravity force) yield higher values of m^* at the OHSD. From Fig. 7b and 8b, it can be concluded that of the parameters studied (r, $\gamma_{H_2,W}$, $\theta_{H_2,W}$, ρ_w and ρ_{H_2}), the values of $h_{working,H_2}$ and m^* are more sensitive to r and $\theta_{H_2,W}$.

In summary, it should be highlighted that OHSD is only affected by $\theta_{H_2,W}$. Moreover, $h_{working,H_2}$ is not noticeably influenced by variations of ρ_{H_2} but varies by the other parameters including r, $\gamma_{H_2,W}$, $\theta_{H_2,W}$, and ρ_w. In particular, $h_{working,H_2}$ is a strong function of r and $\theta_{H_2,W}$. On the other hand, all the parameters studied, specifically r and $\theta_{H_2,W}$, have an impact on m^*.

As mentioned earlier, Iglauer [20] proposed 1100 m as the OHSD and Luboń & Tarkowski [22] reported a range of 1200–1400 m for the OHSD of the Suliszewo structure.

However, in this work we have suggested a depth of about 1600 m with P90 and P10 of 1370 and 1760 m, respectively. It should be noted that previous studies ([20,22]) used different trends for the change of $\theta_{H_2,W}$ as a function of depth and, as discussed before, $\theta_{H_2,W}$ has a large influence on the OHSD. Moreover, the work of Luboń & Tarkowski [22] was carried out with a dynamic simulation where the limits of both capillary and fracture pressure were considered. The work of Luboń & Tarkowski [22] was also based on the specific geological characteristics of the Suliszewo structure, as they also suggested that the OHSD should be evaluated for each specific case. Additionally, there might be unmentioned assumption(s) in the work of Iglauer [20] leading to some breaks in the h_{H_2} and m profiles versus depth, which might affect the value of the OHSD.

Effect of temperature and pressure gradients

To investigate the impacts of T_G and P_G gradients on $h_{working,H_2}$ and m^*, two additional trends were considered. In the first trend, a 25% higher value for P_G was used (0.0125 MPa/m of P_G and 0.03 °C/m of T_G) and in the second one, a 25% higher variation for T_G was assumed (0.01 MPa/m of P_G and 0.0375 °C/m). The parameters ($\gamma_{H_2,W}$, ρ_w and ρ_{H_2}) were changed according to the newly defined T_G and P_G. The evaluations of $h_{working,H_2}$ and m^* were based on the new gradients while the 90° value of $\theta_{H_2,W}$ was assumed to occur at different depths including 3700 m (similar to the base case), 3200 m (for 0.0125 MPa/m and 0.03 °C/m gradients), and 4200 m (for 0.01 MPa/m and 0.0375 °C/m gradients). In all scenarios, the value of $\theta_{H_2,W}$ at the surface was assumed to be 44° and a linear trend was assumed for $\theta_{H_2,W}$ as a function of depth.

Fig. 9 shows the impacts of T_G, P_G, and on $h_{working,H_2}$ and m^*. Fig. 9a shows that similar values for $h_{working,H_2}$ were obtained for different gradients and those of the base case as long as $\theta_{H_2,W}$ was the same. However, when the other trends for $\theta_{H_2,W}$ were used, the $h_{working,H_2}$ values were different at various depths. Higher values for $h_{working,H_2}$ were obtained for the gradients of 0.01 MPa/m and 0.0375 °C/m with 90° value of $\theta_{H_2,W}$ at 4200 m. These results further highlight the very important role of $\theta_{H_2,W}$ in the analysis of structural trapping efficiency. Detailed experimental studies on the values of $\theta_{H_2,W}$ are suggested for the caprock of the targeted underground H_2 site. Moreover, further investigations are recommended to improve the caprock wettability for example through the use of nanofluids [39,58]. Fig. 9b shows the profiles of m^* versus depth with different trends obtained as a result of different $h_{working,H_2}$ and ρ_{H_2} at different gradients. In summary, as long as the same profile was used for $\theta_{H_2,W}$, similar trends were obtained for $h_{working,H_2}$. However, the values of m^* were affected by the variations of ρ_{H_2} due to the different gradients.

Impact of dip angle

Geological structures can have different angles with a horizontal plane, known as dip angle. To investigate the effects of the formation dip angle on the m, a truncated cone was considered to simply represent a subsurface geological formation which is shown in Fig. 10. The structure has a top radius of 1 km. H_2 storage in this structure at 20 and 40° dip angles were studied, and it was assumed that in both cases the reservoir has the required thickness for MHCH. Moreover, similar to the uncertainty quantification section, the base gas was H_2 and thus no CH_4, N_2 or CO_2 was present. In addition, values of 0.2 and 0.25 were considered for ϕ and S_w, respectively.

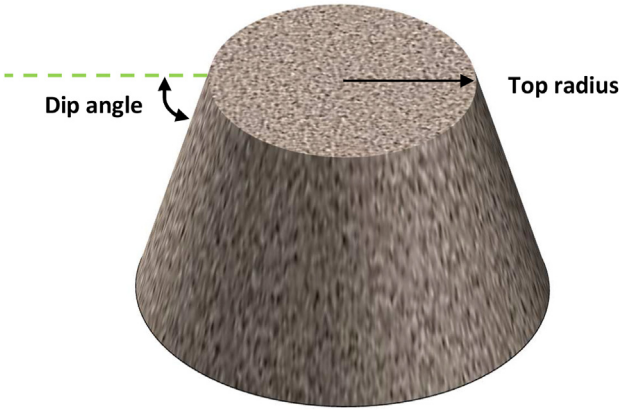

Fig. 10 – Considered truncated cone to study the effect of the dip angle.

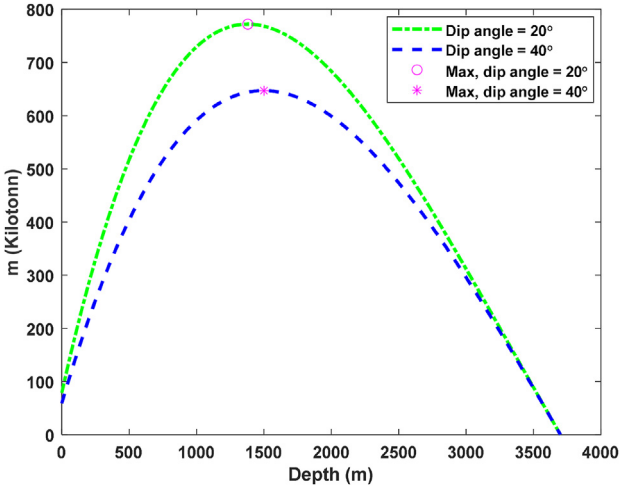

Fig. 11 – The impact of the formation dip angle on m.

It is worth noting that h_{H_2} would be the same for 20° and 40° dip situations. However, larger values of $h_{working,H_2}$ are expected for the case with a formation dip of 40°. This can be explained by the comparatively smaller cross-sectional area at the top of the reservoir for the 40° dip and the need for more height to fill the 50% volume by working gas. Fig. 11 shows the trends of m versus depth for 20° and 40° formation dip. As can be seen in this figure, there was a decrease in the values of m due to the 40° formation dip. At the OHSD, the value of m at a 40° dip is almost 18% lower than at a 20° dip. In summary, although the amount of h_{H_2} does not depend on the slope angle, assuming the same top cross-sectional area, formations with steeper slopes offer less volume and consequently less H_2 can be stored in these formations. A similar result has already been reported for the effect of formation dip on CO_2 storage [59]. Therefore, from a structural trapping point of view, H_2 storage in geological formations with a low dip angle is recommended.

Conclusion

Structural trapping capacity is an important concern associated with hydrogen storage in underground porous formations. In this study, the maximum column height of hydrogen in a geological storage site was formulated to avoid capillary leakage of the stored hydrogen into the caprock. In this formulation, the impacts of other possible base gases such as nitrogen, carbon dioxide, and hydrocarbon gas were considered. Normal temperature and pressure gradients of 0.01 MPa/m and 0.03 °C/m were used, respectively, and the mean pore radius of the caprock was 50 nm. Representative experimental data and correlations were then used to calculate the required rock and fluid properties as a function of depth. Particularly, hydrogen-water contact angle was assumed to change linearly from 44° at surface to 90° at 3700 m depth. The maximum column height and storable mass of the hydrogen per effective pore area (m^*) in aquifers and depleted gas reservoirs were determined. The findings can be summarized in the following points.

- Based on the assumed trend of hydrogen-water contact angle, the optimum depths for hydrogen storage in aquifers when hydrogen, nitrogen, and carbon dioxide function as base gases are 1605, 1660, and 1630 m, respectively.
- In depleted gas reservoirs, the contribution of the remaining hydrocarbon gas such as methane in the base gas, does not noticeably change the optimum storage depths.
- A higher density gas enhances the gravity force, which acts against the buoyancy force. This in turn allows for a higher hydrogen column height and m^*. The values obtained for the optimum m^* of the cases with carbon dioxide, nitrogen, and hydrogen as the base gas are 835, 643, and 599 kg/m^2, respectively.
- In gas reservoirs, the use of nitrogen in addition to the remaining hydrocarbon gas (methane), would not considerably affect the maximum height and m^*. This is different for carbon dioxide due to its high density.
- Uncertainty assessment using Monte Carlo simulation with triangular distributions for the parameters involved, showed that P10, P50, and P90 of the optimum depths are 1760, 1565, and 1370 m, respectively (in aquifers and when hydrogen is the base gas). Moreover, the m^* at the optimum depths of P10, P50, and P90 is 872, 515, and 310 kg/m^2, respectively.
- A sensitivity analysis was performed for contact angle, interfacial tension, cap rock pore radius, and water and hydrogen densities. The results showed that the contact angle and the caprock pore radius have a greater influence on the maximum height and m^*. In addition, the results revealed that only the contact angle affects the optimum storage depth. Moreover, the results of the impacts of temperature and pressure gradients and contact angle profiles, further emphasized the importance of the contact angle on the maximum height and m^*.
- Mixing can decrease the values of the maximum height and m^* when carbon dioxide as a base gas mixes with a remaining hydrocarbon gas (methane) or with hydrogen, as this results in a base gas with a lower density.
- A truncated cone was assumed to be representative of a subsurface geological formation with a constant top cross-sectional area and 20° and 40° dip angles. It was also assumed that in both cases, the formation has the necessary thickness for the maximum hydrogen column height at different depths. The results showed that the formation dip angle can influence the amount of hydrogen mass that can be stored. For the assumed structure, the formations with a steeper dip angle offer less volume and thus less hydrogen can be stored in such formations.

Declaration of competing interest

The authors declare that they have no known competing financial interests or personal relationships that could have appeared to influence the work reported in this paper.

Appendixes A and B. Supplementary data

Supplementary data to this article can be found online at https://doi.org/10.1016/j.ijhydene.2023.07.071.

REFERENCES

[1] Liu F, Mauzerall DL, Zhao F, Hao H. Deployment of fuel cell vehicles in China: greenhouse gas emission reductions from converting the heavy-duty truck fleet from diesel and natural gas to hydrogen. Int J Hydrogen Energy 2021;46:17982–97. https://doi.org/10.1016/J.IJHYDENE.2021.02.198.

[2] Pal DB, Singh A, Bhatnagar A. A review on biomass based hydrogen production technologies. Int J Hydrogen Energy 2022;47:1461–80. https://doi.org/10.1016/J.IJHYDENE.2021.10.124.

[3] Pandey AP, Bhatnagar A, Shukla V, Soni PK, Singh S, Verma SK, et al. Hydrogen storage properties of carbon aerogel synthesized by ambient pressure drying using new catalyst triethylamine. Int J Hydrogen Energy 2020;45:30818–27. https://doi.org/10.1016/J.IJHYDENE.2020.08.145.

[4] Hassanpouryouzband A, Joonaki E, Edlmann K, Haszeldine RS. Offshore geological storage of hydrogen: is this our best option to achieve net-zero? ACS Energy Lett 2021;6:2181–6. https://doi.org/10.1021/acsenergylett.1c00845.

[5] Heinemann N, Scafidi J, Pickup G, Thaysen EM, Hassanpouryouzband A, Wilkinson M, et al. Hydrogen storage in saline aquifers: the role of cushion gas for injection and production. Int J Hydrogen Energy 2021;46:39284–96. https://doi.org/10.1016/j.ijhydene.2021.09.174.

[6] Tarkowski R, Uliasz-Misiak B. Towards underground hydrogen storage: a review of barriers. Renew Sustain Energy Rev 2022;162:112451. https://doi.org/10.1016/j.rser.2022.112451.

[7] Andersson J, Grönkvist S. Large-scale storage of hydrogen. Int J Hydrogen Energy 2019;44:11901–19. https://doi.org/10.1016/j.ijhydene.2019.03.063.

[8] Zivar D, Kumar S, Foroozesh J. Underground hydrogen storage: a comprehensive review. Int J Hydrogen Energy 2021;46:23436–62. https://doi.org/10.1016/j.ijhydene.2020.08.138.
[9] Lankof L, Urbańczyk K, Tarkowski R. Assessment of the potential for underground hydrogen storage in salt domes. Renew Sustain Energy Rev 2022;160. https://doi.org/10.1016/j.rser.2022.112309.
[10] Lysyy M, Fernø M, Ersland G. Seasonal hydrogen storage in a depleted oil and gas field. Int J Hydrogen Energy 2021;46:25160–74. https://doi.org/10.1016/j.ijhydene.2021.05.030.
[11] Williams JDO, Williamson JP, Parkes D, Evans DJ, Kirk KL, Sunny N, et al. Does the United Kingdom have sufficient geological storage capacity to support a hydrogen economy? Estimating the salt cavern storage potential of bedded halite formations. J Energy Storage 2022;53:105109. https://doi.org/10.1016/j.est.2022.105109.
[12] Bai T, Tahmasebi P. Coupled hydro-mechanical analysis of seasonal underground hydrogen storage in a saline aquifer. J Energy Storage 2022;50:104308. https://doi.org/10.1016/j.est.2022.104308.
[13] Luboń K, Tarkowski R. Numerical simulation of hydrogen injection and withdrawal to and from a deep aquifer in NW Poland. Int J Hydrogen Energy 2020;45:2068–83. https://doi.org/10.1016/j.ijhydene.2019.11.055.
[14] Lankof L, Tarkowski R. Assessment of the potential for underground hydrogen storage in bedded salt formation. Int J Hydrogen Energy 2020;45:19479–92. https://doi.org/10.1016/j.ijhydene.2020.05.024.
[15] Ali M, Pan B, Yekeen N, Al-Anssari S, Al-Anazi A, Keshavarz A, et al. Assessment of wettability and rock-fluid interfacial tension of caprock: implications for hydrogen and carbon dioxide geo-storage. Int J Hydrogen Energy 2022;47:14104–20. https://doi.org/10.1016/j.ijhydene.2022.02.149.
[16] Zeng L, Vialle S, Ennis-King J, Esteban L, Sarmadivaleh M, Sarout J, et al. Role of geochemical reactions on caprock integrity during underground hydrogen storage. SSRN Electron J 2022. https://doi.org/10.2139/SSRN.4233860.
[17] Hosseini M, Fahimpour J, Ali M, Keshavarz A, Iglauer S. Hydrogen wettability of carbonate formations: implications for hydrogen geo-storage. J Colloid Interface Sci 2022;614:256–66. https://doi.org/10.1016/j.jcis.2022.01.068.
[18] Ghaedi M, Andersen PØ, Gholami R. Hydrogen diffusion into caprock: a semi-analytical solution and a hydrogen loss criterion. J Energy Storage 2023;64:107134. https://doi.org/10.1016/J.EST.2023.107134.
[19] Li Z, Dong M, Li S, Huang S. CO2 sequestration in depleted oil and gas reservoirs-caprock characterization and storage capacity. Energy Convers Manag 2006;47:1372–82. https://doi.org/10.1016/J.ENCONMAN.2005.08.023.
[20] Iglauer S. Optimum geological storage depths for structural H2 geo-storage. J Pet Sci Eng 2022;212:109498. https://doi.org/10.1016/j.petrol.2021.109498.
[21] Alessa S, Sakhaee-Pour A, Alipour M. Safe pressure for hydrogen storage in subsurface. Energy Rep 2022;8:15702–11. https://doi.org/10.1016/J.EGYR.2022.11.141.
[22] Luboń K, Tarkowski R. The influence of the first filling period length and reservoir level depth on the operation of underground hydrogen storage in a deep aquifer. Int J Hydrogen Energy 2022. https://doi.org/10.1016/J.IJHYDENE.2022.09.284.
[23] Espinoza DN, Santamarina JC. CO2 breakthrough—caprock sealing efficiency and integrity for carbon geological storage. Int J Greenh Gas Control 2017;66:218–29. https://doi.org/10.1016/J.IJGGC.2017.09.019.
[24] Iglauer S. Optimum storage depths for structural CO2 trapping. Int J Greenh Gas Control 2018;77:82–7. https://doi.org/10.1016/J.IJGGC.2018.07.009.
[25] Ma J, Li Q, Kempka T, Kühn M. Hydromechanical response and impact of gas mixing behavior in subsurface CH4 Storage with CO2-based cushion gas. Energy Fuel 2019;33:6527–41. https://doi.org/10.1021/acs.energyfuels.9b00518.
[26] MATLAB. Natick. Massachusetts: The MathWorks Inc.; 2022.
[27] Chow YTF, Maitland GC, Trusler JPM. Interfacial tensions of (H2O + H2) and (H2O + CO2 + H2) systems at temperatures of (298–448) K and pressures up to 45 MPa. Fluid Phase Equil 2018;475:37–44. https://doi.org/10.1016/J.FLUID.2018.07.022.
[28] Hosseini M, Fahimpour J, Ali M, Keshavarz A, Iglauer S. H2–brine interfacial tension as a function of salinity, temperature, and pressure; implications for hydrogen geo-storage. J Pet Sci Eng 2022;213:110441. https://doi.org/10.1016/J.PETROL.2022.110441.
[29] Al-mukainah H, Al-yaseri A, Yekeen N, Al J. Wettability of shale – brine – H 2 system and H 2 -brine interfacial tension for assessment of the sealing capacities of shale formations during underground hydrogen storage. Energy Rep 2022;8:8830–43. https://doi.org/10.1016/j.egyr.2022.07.004.
[30] Ali M, Yekeen N, Pal N, Keshavarz A, Iglauer S, Hoteit H. Influence of pressure, temperature and organic surface concentration on hydrogen wettability of caprock; implications for hydrogen geo-storage. Energy Rep 2021;7:5988–96. https://doi.org/10.1016/J.EGYR.2021.09.016.
[31] Al-Yaseri A, Yekeen N, Mahmoud M, Kakati A, Xie Q, Giwelli A. Thermodynamic characterization of H2-brine-shale wettability: implications for hydrogen storage at subsurface. Int J Hydrogen Energy 2022;47:22510–21. https://doi.org/10.1016/j.ijhydene.2022.05.086.
[32] Esfandyari H, Sarmadivaleh M, Esmaeilzadeh F, Ali M, Iglauer S, Keshavarz A. Experimental evaluation of rock mineralogy on hydrogen-wettability: implications for hydrogen geo-storage. J Energy Storage 2022;52:104866. https://doi.org/10.1016/j.est.2022.104866.
[33] Hashemi L, Glerum W, Farajzadeh R, Hajibeygi H. Contact angle measurement for hydrogen/brine/sandstone system using captive-bubble method relevant for underground hydrogen storage. Adv Water Resour 2021;154:103964. https://doi.org/10.1016/j.advwatres.2021.103964.
[34] Iglauer S, Ali M, Keshavarz A. Hydrogen wettability of sandstone reservoirs: implications for hydrogen geo-storage. Geophys Res Lett 2021;48:e2020GL090814. https://doi.org/10.1029/2020GL090814.
[35] Zeng L, Hosseini M, Keshavarz A, Iglauer S, Lu Y, Xie Q. Hydrogen wettability in carbonate reservoirs: implication for underground hydrogen storage from geochemical perspective. Int J Hydrogen Energy 2022;47:25357–66. https://doi.org/10.1016/j.ijhydene.2022.05.289.
[36] Aslannezhad M, Ali M, Kalantariasl A, Sayyafzadeh M, You Z, Iglauer S, et al. A review of hydrogen/rock/brine interaction: implications for Hydrogen Geo-storage. Prog Energy Combust Sci 2023;95:101066. https://doi.org/10.1016/J.PECS.2022.101066.
[37] Ali M, Yekeen N, Pal N, Keshavarz A, Iglauer S, Hoteit H. Influence of organic molecules on wetting characteristics of mica/H2/brine systems: implications for hydrogen structural trapping capacities. J Colloid Interface Sci 2022;608:1739–49. https://doi.org/10.1016/J.JCIS.2021.10.080.
[38] Hosseini M, Fahimpour J, Ali M, Keshavarz A, Iglauer S. Capillary sealing efficiency analysis of caprocks: implication for hydrogen geological storage. Energy Fuel 2022;36:4065–75. https://doi.org/10.1021/acs.energyfuels.2c00281.

[39] Alanazi A, Ali M, Mowafi M, Hoteit H. Effect of organics and nanofluids on capillary-sealing efficiency of caprock for hydrogen and carbon-dioxide geological storage. 2022. https://doi.org/10.56952/IGS-2022-009.
[40] Alanazi A, Yekeen N, Ali M, Ali M, Abu-Mahfouz IS, Keshavarz A, et al. Influence of organics and gas mixing on hydrogen/brine and methane/brine wettability using Jordanian oil shale rocks: implications for hydrogen geological storage. J Energy Storage 2023;62:106865. https://doi.org/10.1016/J.EST.2023.106865.
[41] Al-Yaseri A, Abdulelah H, Yekeen N, Ali M, Negash BM, Zhang Y. Assessment of CO2/shale interfacial tension. Colloids Surf A Physicochem Eng Asp 2021;627:127118. https://doi.org/10.1016/J.COLSURFA.2021.127118.
[42] Esfandyari H, Hosseini M, Ali M, Iglauer S, Haghighi M, Keshavarz A. Assessment of the interfacial properties of various mineral/hydrogen/water systems. J Energy Storage 2023;60:106637. https://doi.org/10.1016/J.EST.2023.106637.
[43] Yekeen N, Al-Yaseri A, Negash BM, Ali M, Giwelli A, Esteban L, et al. Clay-hydrogen and clay-cushion gas interfacial tensions: implications for hydrogen storage. Int J Hydrogen Energy 2022;47:19155–67. https://doi.org/10.1016/J.IJHYDENE.2022.04.103.
[44] Hosseini M, Ali M, Fahimpour J, Keshavarz A, Iglauer S. Assessment of rock-hydrogen and rock-water interfacial tension in shale, evaporite and basaltic rocks. J Nat Gas Sci Eng 2022;106:104743. https://doi.org/10.1016/J.JNGSE.2022.104743.
[45] Alanazi A, Rasool Abid H, Usman M, Ali M, Keshavarz A, Vahrenkamp V, et al. Hydrogen, carbon dioxide, and methane adsorption potential on Jordanian organic-rich source rocks: implications for underground H2 storage and retrieval. Fuel 2023;346:128362. https://doi.org/10.1016/J.FUEL.2023.128362.
[46] Generous MM, Qasem NAA, Qureshi BA, Zubair SM. A comprehensive review of saline water correlations and data-Part I: thermodynamic properties. Arabian J Sci Eng 2020;45:8817–76. https://doi.org/10.1007/s13369-020-05020-5.
[47] Nayar KG, Sharqawy MH, Banchik LD, Lienhard JH. Thermophysical properties of seawater: a review and new correlations that include pressure dependence. Desalination 2016;390:1–24. https://doi.org/10.1016/J.DESAL.2016.02.024.
[48] Leachman JW, Jacobsen RT, Penoncello SG, Lemmon EW. Fundamental equations of state for parahydrogen, normal hydrogen, and orthohydrogen. J Phys Chem Ref Data 2009;38:721–48. https://doi.org/10.1063/1.3160306.
[49] Setzmann U, Wagner W. A new equation of state and tables of thermodynamic properties for methane covering the range from the melting line to 625 K at pressures up to 1000 MPa. J Phys Chem Ref Data 1991;20:1061–155. https://doi.org/10.1063/1.555898.
[50] Span R, Lemmon EW, Jacobsen RT, Wagner W, Yokozeki A. A reference equation of state for the thermodynamic properties of nitrogen for temperatures from 63.151 to 1000 K and pressures to 2200 MPa. J Phys Chem Ref Data 2000;29:1361–433. https://doi.org/10.1063/1.1349047.
[51] Span R, Wagner W. A new equation of state for carbon dioxide covering the fluid region from the triple-point temperature to 1100 K at pressures up to 800 MPa. J Phys Chem Ref Data 1996;25:1509–96. https://doi.org/10.1063/1.555991.
[52] Van Der Meer B. Carbon dioxide storage in natural gas reservoirs. Oil & Gas Science and Technology-Rev IFP 2005;60:527–36. https://doi.org/10.2516/ogst:2005035.
[53] Sadeghi S, Sedaee B. Cushion and working gases mixing during underground gas storage: role of fractures. J Energy Storage 2022;55:105530. https://doi.org/10.1016/J.EST.2022.105530.
[54] Mehana M, Callard J, Kang Q, Viswanathan H. Monte Carlo simulation and production analysis for ultimate recovery estimation of shale wells. J Nat Gas Sci Eng 2020;83:103584. https://doi.org/10.1016/J.JNGSE.2020.103584.
[55] Kok MV, Kaya E, Akin S. Monte Carlo simulation of oil fields. Energy Sources B Energy Econ Plann 2006;1:207–11. https://doi.org/10.1080/15567240500400770.
[56] Zaremoayedi F, Ghaedi M, Kazemi N. A new approach to production data analysis of non-volumetric naturally fractured gas condensate reservoirs. J Nat Gas Sci Eng 2022;105:104703. https://doi.org/10.1016/J.JNGSE.2022.104703.
[57] Fazlollahtabar H. Triple state reliability measurement for a complex autonomous robot system based on extended triangular distribution. Measurement 2019;139:122–6. https://doi.org/10.1016/J.MEASUREMENT.2019.02.016.
[58] Ali M, Sahito MF, Jha NK, Arain ZUA, Memon S, Keshavarz A, et al. Effect of nanofluid on CO2-wettability reversal of sandstone formation; implications for CO2 geo-storage. J Colloid Interface Sci 2020;559:304–12. https://doi.org/10.1016/J.JCIS.2019.10.028.
[59] Wang F, Jing J, Xu T, Yang Y, Jin G. Impacts of stratum dip angle on CO2 geological storage amount and security. Greenhouse Gases: Sci Technol 2016;6:682–94. https://doi.org/10.1002/GHG.1594.